SAND2022-17041C

CO_2-Enhanced Filtered Rayleigh Scattering for Study of a Hypersonic Cone-Slice-Ramp Geometry

Ashley J. Saltzman*, Anshuman Pandey†, Steven J. Beresh‡, Katya M. Casper§, Rajkumar Bhakta**, Brian P. Denk††, Marie E. De Zetter‡‡, and Russell W. Spillers§§
Sandia National Laboratories, Albuquerque, New Mexico 87185

This work applies Filtered Rayleigh Scattering (FRS) for the study of shock wave/boundary layer interactions on a cone-slice-ramp geometry. As FRS measures a planar slice of the flow, the three-dimensionality of this geometry can be captured, rather than path-integrated imaging such as schlieren. A carbon dioxide seeding system designed for the Sandia Hypersonic Wind Tunnel provides sufficient light scattering for FRS measurements. Strong background rejection in the images was achieved using a molecular gas filter, resulting in detailed visualization of flow structures within the boundary and shear layers. Images show turbulence transition, as well as flow instabilities and reattachment on the ramp. A highly unsteady separation region was investigated, showing instantaneous shaping of the shock structure with turbulence.

I. Introduction

HYPERSONIC bodies are subjected to multiple fluid-structure interactions which disturb the body and cause vibrations. Flow over an expansion or compression corner can produce or modify boundary layer instabilities, driving transition to turbulence and increased heat flux and pressure loading [1]. While two-dimensional expansion or compression geometries have been widely researched to investigate shock wave/boundary layer interactions (SWBLI), further study is needed of non-canonical geometries to understand implications for flight [2].

* Senior Member of the Technical Staff, Asset Security Center, Member AIAA
† Senior Member of the Technical Staff, Engineering Sciences Center, Member AIAA
‡ Distinguished Member of the Technical Staff, Engineering Sciences Center, Associate Fellow AIAA
§ Principal Member of the Technical Staff, Engineering Sciences Center, Associate Fellow AIAA
** Senior Test Operations Engineer, Engineering Sciences Center
†† Senior Technologist, Engineering Sciences Center
‡‡ Senior Technologist, Engineering Sciences Center
§§ Principal Technologist, Engineering Sciences Center

Boundary layer transition in slender cones typically begins with linear instability growth [3]. For higher Mach numbers, the second mode dominates instability mechanisms leading to transition [4]. A non-canonical three-dimensional cone-slice-ramp geometry has recently been deployed in Sandia's Hypersonic Wind Tunnel (HWT) to study three-dimensional SWBLI and fluid-structure interactions [5, 6]. The model geometry, shown in Fig. 1, consists of a 7° half-angle slender cone with a longitudinal cut creating a slice, upon which ramps of different angles can be mounted for study. In an expansion only case (no ramp), high-frequency surface pressure and schlieren measurements have shown second-mode waves rapidly decay along the slice, while lower frequency instability waves grow. In that case, the expansion actually delays boundary-layer transition. With the addition of a 30° ramp, flow separation is induced, and second-mode waves propagate along the separated shear layer. Additionally, medium to low frequency disturbances were observed within the separation bubble using surface pressure sensors. The current work seeks to improve understanding of SWBLI on this geometry using a planar imaging technique.

Spatially resolved images are desirable to help explain fluid mechanics phenomena observed from pressure sensor data. Path integrated flow visualization techniques, like schlieren or shadowgraph, are widespread in the study of fluid dynamics. However, these techniques may be misleading for highly three-dimensional flows, such as the model geometries of interest to the current work. The images from these techniques contain information from flow structures throughout the entire measurement depth (path), so it is difficult to discern at which spanwise position the features originate. In contrast, planar laser scattering (PLS) techniques provide the ability to observe a slice of the flow. The features observed in these planar images can be attributed to specific spanwise positions, allowing for a clearer interpretation of features. Additionally, the location of this plane can then be traversed to obtain a realistic understanding of the three-dimensional flow-field. Among these techniques is planar particle image velocimetry (PIV), which relies on scattering from relatively large particles in the Mie scattering regime. This technique has become widespread in fluid dynamics research [7, 8]; however, the required larger particles are unsuitable for hypersonic flows, as they will suffer from particle lag in regions with large velocity gradients. Doppler global velocimetry (DGV) relies on the principle of the Doppler shift to determine velocity by measuring the change in light frequency due to a flow [9]. Unlike PIV, DGV is functional with particles of any size with sufficient light scattering signals. Thus, particles much smaller than the laser wavelength, such as flow molecules or added condensates, could be used. Due to their small size, these particles in the Rayleigh regime do not experience lag in regions of strong velocity gradients and are therefore suitable for hypersonic flow measurements.

Since the molecular Rayleigh scattering signal is weaker than Mie and background scattering [10], researchers have previously added condensate – water, alcohol, or carbon dioxide (CO_2) – to enhance the scattering signal. Particles condense during the nozzle expansion to scatter light and reveal turbulent structures and shocks, which can be seen in Refs. [11-14], to name a few examples. Recently, a CO_2 flow seeding system has been developed and demonstrated in the Sandia Hypersonic Wind Tunnel (HWT) [15]. Using the seeding system for CO_2-enhanced PLS revealed details of turbulence transition in the boundary layer and wake of a sharp-nosed cone in Mach 8 flow. Suspected second-mode waves, the wake recompression shock, and expansion wave were also observed in the PLS images. Compared to time-averaged schlieren images obtained in the flow, the PLS better visualized details of the flow structure, which would be valuable for studying SWBLI mechanisms in the current application. Further, background-scattered light can be suppressed using a molecular gas filter, enabling better imaging results through a technique known as Filtered Rayleigh Scattering (FRS) [16].

The current work seeks to use CO_2-enhanced FRS for flow characterization of the non-canonical three-dimensional cone-slice-ramp geometry. The 30° ramp configuration is used to induce and study flow separation. FRS images of the geometry at a variety of Reynolds numbers are presented and show detailed visualization of boundary layer characteristics, transition, and separated flow, with comparisons to schlieren images. The effect of the background suppression is also studied by comparing FRS images to simultaneous PLS for varying Reynolds numbers. This paper is organized as follows: Sect. II provides details on the facility, model geometry, and experimental setup of the FRS imaging, Sect. III shows resulting images of FRS and schlieren of the model, and Sect. IV concludes the paper and discusses future work.

II. Methods

A. Hypersonic Wind Tunnel Facility

Testing was performed in the Sandia Hypersonic Wind Tunnel (HWT), a blowdown-to-vacuum facility using interchangeable nozzles and heaters to enable test section Mach numbers of 5, 8, or 14. The current work used only the Mach 8 configuration, which has a 355.6 mm diameter axisymmetric test section and uses nitrogen gas as the working fluid. Tunnel run times up to 60 seconds long are possible, with a turnaround time of 45 minutes between runs. Additional facility details can be found in Refs. [17, 18].

A liquid CO_2 seeding system was previously designed and installed in the HWT to facilitate flow visualization by enhanced Rayleigh scattering [15]. In the system, high pressure helium is used to extract liquid CO_2 from six supply

bottles. The quantity of CO_2 is adjusted manually via a needle valve prior to each run, based on the run conditions. The seeder can supply up to 2.7 gallons of liquid CO_2 per minute, approximately 1-2% by mass of HWT flow. During a run, the seeder flow is controlled remotely by a LabVIEW program via a solenoid valve. The liquid CO_2 is injected through a spray nozzle into the nitrogen supply upstream of the heater section. The CO_2 fully evaporates prior to entering the heater section, necessary to prevent damage to the heater screens. Expansion through the nozzle causes the gaseous CO_2 to condense into particles expected to be approximately 10 nm in diameter [11, 19], which can then scatter light in the test section and enable PLS or FRS. The CO_2 seeding system was designed and tested for Mach 8 flow but will eventually be upgraded to support different Mach numbers.

B. Cone-slice-ramp Model

The test model is a sharp-nosed 7° half-angle cone, shown in Fig. 1. The cone has a longitudinal cut which creates a slice at the aft end. Different spanwise ramps with a variety of angles can be mounted on the slice. This model, with ramps of 0° (flat plate), 10°, 20°, and 30°, has been studied in the HWT using high-speed schlieren [5, 6], high-frequency pressure sensors [5, 6], focused laser differential interferometry (FLDI) [5], and digital image correlation (DIC) [20]. In the current work, only the 30° ramp was used to induce flow separation interactions for study by FRS. All testing was conducted at zero angle of attack, and the model is sting-mounted at the base of the cone.

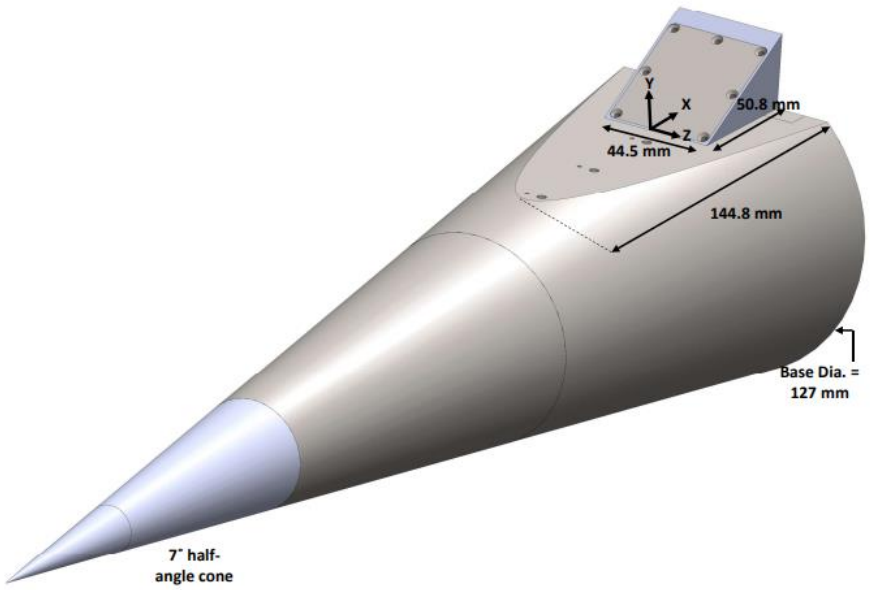

Fig. 1 Schematic of the cone-slice-ramp model geometry used in the current work, shown with a 30° ramp.

C. Filtered Rayleigh Scattering Measurement

To study SWBLI, an FRS measurement was implemented in the HWT. For velocimetry, FRS relies on measuring the Doppler shift, described by the following equation,

$$\Delta f_D = \frac{\vec{U} \cdot (\hat{o} - \hat{\imath})}{\lambda} \tag{1}$$

where $\vec{U}$ is the flow velocity vector, $\hat{o}$ is the direction of camera observation, $\hat{\imath}$ is the incident laser direction, and λ is the incident laser wavelength. The frequency of the laser light is typically determined by observing the transmission through a molecular gas filter of iodine. The transmission of 532 nm light through iodine gas has been well-characterized [21]. A precise wavelength meter, if available, can also be used for frequency monitoring; however, the shifted frequency in the images must be determined using a gas filter. In practice, determining the shifted laser frequency can be difficult in hypersonic flows with large Doppler shifts. Researchers have investigated variations to the conventional DGV method to increase dynamic range, such as cross-correlation DGV [22], which may facilitate measurements in hypersonic flows [23]. In the present work, velocity is used only to discriminate signal, as background scattering originates from stationary wind tunnel and model surfaces.

The Rayleigh scattering signal is dependent on the temperature and pressure of molecules in the flow. The Rayleigh lineshape is commonly estimated based on the models developed by Tenti et al. [24] and Pan et al. [25]. Thus, the observed signal in a typical FRS measurement will be the convolution of the Rayleigh lineshape, any Mie scattering signal, the background (geometric) scattering signal, and the absorption spectrum of the gas filter [16]. Implementation of FRS and its use for determining velocity have been previously described by several other works [16, 26-29]. However, in the current application, velocity can be determined from Eq. 1, since particle scattering, such as that from CO_2 condensate, does not experience temperature broadening.

The FRS measurement offers distinct advantages over PLS. Since the Doppler shift can be quantified using a molecular gas filter, quantitative measurements of velocity are possible given sufficient signal in the images. This implementation is usually known as DGV. Additionally, while PLS images can suffer from laser flare and reflections, FRS images can reject background scattering using a molecular gas filter. By frequency tuning the laser to a region of high absorption by the iodine cell, shown by Fig. 2(a), the background light scattering will be suppressed, as it will not experience a Doppler shift. However, high-speed flows studied by the current work will cause a Doppler shift to lower wavenumbers (higher transmission) by the cell, Fig. 2(b). This background suppression will greatly improve

the signal-to-noise ratio in the images, and it may also reveal additional flow details. While this simpler implementation of FRS improves image quality, it does not provide velocimetry.

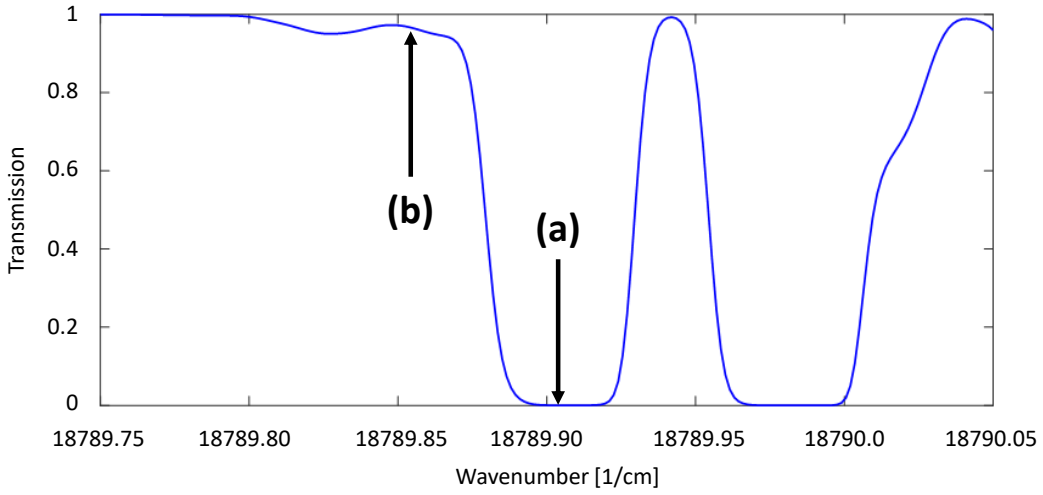

Fig. 2 Model iodine absorption spectrum showing (a) region of high absorption by the cell and (b) resulting Doppler-shifted transmission for high velocity.

D. Imaging Experiment and Flow Conditions

An FRS imaging system was used to study the three-dimensional cone-slice-ramp geometry. The experimental setup of the FRS measurement is shown in Fig. 3. First, a laser conditioning subsystem, Fig. 3(a), is used to monitor the incident laser frequency during the run. This measurement used a 10-Hz Nd:YAG laser system (QuantaRay PIV-400). The QuantaRay provides approximately 220 mJ/pulse of 532 nm light, with pulse widths of approximately 12 ns. Figure 3 shows the laser beam (1) is split by a polarizing beamsplitter with an 80/20 ratio (2). The primary beam is directed to the wind tunnel test section, while the secondary beam is used for frequency monitoring. It is divided by a second beamsplitter with a 50/50 ratio (3), where part of the beam is filtered by an iodine cell (4) and observed by a photodiode (5). The second part of the beam is observed directly as the reference signal (6). In Fig. 3(b), the test model is shown in the wind tunnel test section (7). An sCMOS camera (8, pco.Edge 5.5) observes the model through a second iodine filter (9). An additional sCMOS camera (10) is placed next to the filtered camera as a reference measurement (PLS) with a similar observation angle. Each sCMOS camera operates at 10 Hz, synchronized with the laser pulses. In Fig. 3(c), a side view of the test section shows the laser expanded through a cylindrical lens with a focal length of -10.1 mm (11) to form a 200-mm wide laser sheet (12). The field-of-view of the cameras (13) is seen to observe the expansion corner, slice, and ramp of the model (14).

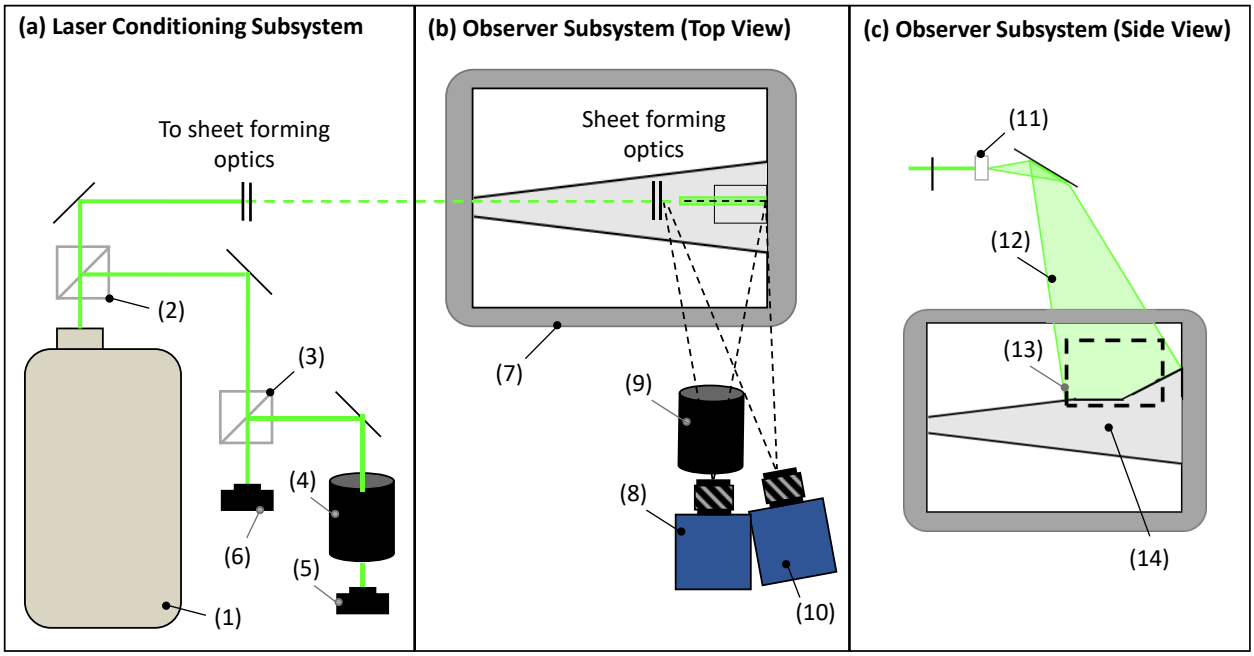

Fig. 3 Drawing of the experimental setup for FRS (a) Laser conditioning subsystem for frequency monitoring. (b) Top view of the wind tunnel test section showing test model and camera configuration. (c) Side view of the test section showing sheet forming optics and cone-slice-ramp model. Number labels are discussed in the text and drawing is not to scale.

For each run, the cameras were triggered after reaching the desired tunnel operating condition. At the same time, the seeding system opens the CO_2 solenoid valve. The CO_2 flows for 7 seconds, then the solenoid valve is closed. This timing was chosen to maximize the amount of tunnel runs possible before needing to replace the CO_2 supply bottles. The FRS images are acquired for 10 seconds, longer than the 7-second CO_2 flow time to ensure full capture of the light scattering time period, resulting in 100 images per run. A wide range of Reynolds numbers, *Re*, was explored to characterize the effect on the boundary layer of the cone-slice-ramp. The tunnel conditions are summarized in Table 1, with P_0 and T_0 referring to the tunnel stagnation pressure and temperature, respectively. While the FRS and schlieren images were not collected at identical run conditions, the pairs closest in Reynolds number will be compared qualitatively in Sect. III.

Table 1 Summary of wind tunnel conditions used in FRS study of cone-slice-ramp geometry.

Diagnostic	T_0 [K]	P_0 [kPa]	Re [1/m]
FRS	2068	733	4.3×10^6
FRS	2758	606	7.6×10^6
FRS	3723	611	10.1×10^6
FRS	4068	611	10.9×10^6
FRS	4413	611	12.0×10^6
Schlieren	2386	803	4.6×10^6
Schlieren	2579	621	7.4×10^6
Schlieren	2875	574	9.3×10^6
Schlieren	5771	682	14.0×10^6

III. Results and Discussion

This section presents images of the boundary layer and separation shear layer of the cone-slice-ramp geometry obtained by FRS for a wide range of Reynolds numbers. The FRS images shown in this section have been processed to remove the vignetting-like effect caused by reflection within the iodine cell. The reference images were dewarped to match the filtered camera coordinates. In total, 100 images were collected by each camera. In a separate set of runs, schlieren images were collected at a framerate of 100 kHz. The averages of these path-integrated schlieren images are also shown in this section for comparison with the planar FRS measurements.

First, Fig. 4 compares the reference PLS image, 4(a), to the filtered image, 4(b), to assess the background suppression achieved with the iodine cell for both low and high Reynolds numbers. The coordinate system placed the origin at the onset of the cone's slice, and the solid white line indicates the surface wall of the cone. In the images, light scatters off the condensed CO_2 to visualize the freestream, the conical shock from the model nose tip, and the separation shock. Near the wall, the increased temperature evaporates the CO_2 particles, resulting in the clearly visible boundary and shear layers observed in Fig. 4. The arc segment structure which stretches approximately vertical from $x = -10$ mm in the filtered images, Fig. 4(b), is a reflection from the iodine cell and not a flow feature. The reference images show strong light scattering off the model, which saturates the camera pixels closest to the surface and obscures the size of the boundary and shear layers. Strong background intensity is also shown in the upper left corner of these reference images, caused by a reflection of the wind tunnel windows. The flow reattachment along the ramp is not visible in the reference images, since the camera was angled slightly behind the ramp, blocking the view. The iodine-filtered images, Fig. 4(b), are noticeably darker than the reference images. This is expected since the flow velocity causes a Doppler shift to a region of higher transmission. Since the model and background are not moving, these

regions do not experience a shift, so the light scattering is suppressed. Consequently, the true size of the boundary and shear layers is better revealed by the filtered images, as the surface of the model is visible. The image contrast is also much improved. Overall, the use of FRS in the measurement, rather than PLS, provides much better flow visualization and opportunities for quantitative results.

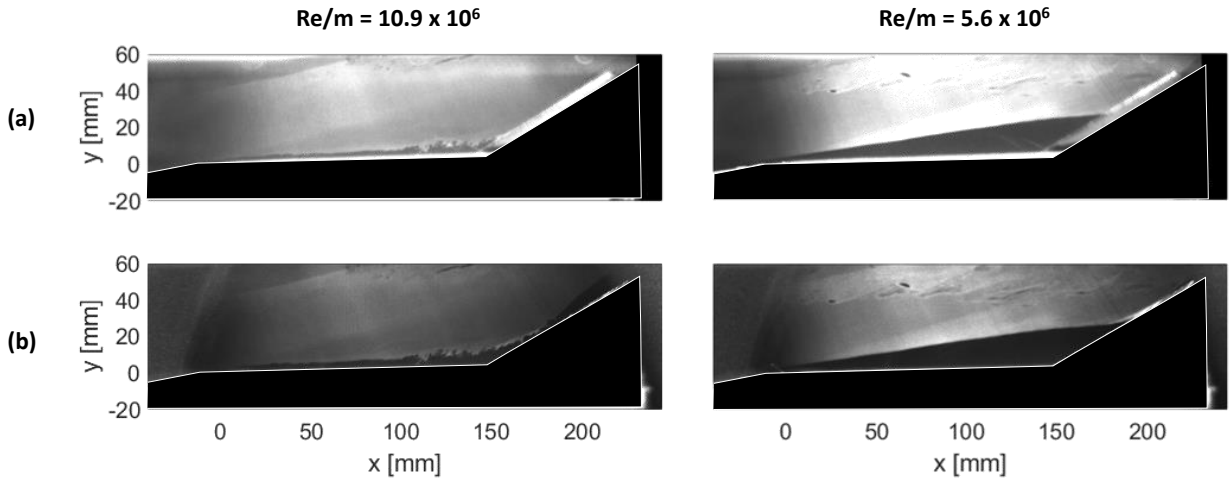

Fig. 4 Comparison of reference (a) and filtered (b) cameras for Re/m (left) 10.9 × 10^6 and (right) 5.6 × 10^6. The solid white line indicates the surface of the model.

Although only 100 FRS images were obtained per run, an average measurement is first desired to study overall trends with changes in Reynolds number. To ensure only images with sufficient light scattering by CO_2 were included, the average image intensity through time was interrogated. The average intensity from one column within the images, marked in Fig. 5(a), was plotted through time in Fig. 5(b). A general increase in intensity can be observed starting near 1 second, which persists for approximately 8 seconds. Since the CO_2 solenoid valve was opened at 0 seconds, and closed after 7 seconds, this intensity increase can be attributed to CO_2 condensation, which requires some time for buildup. To find the average image, the instantaneous images were bounded between 1 – 8 seconds for the computation, corresponding to 70 images.

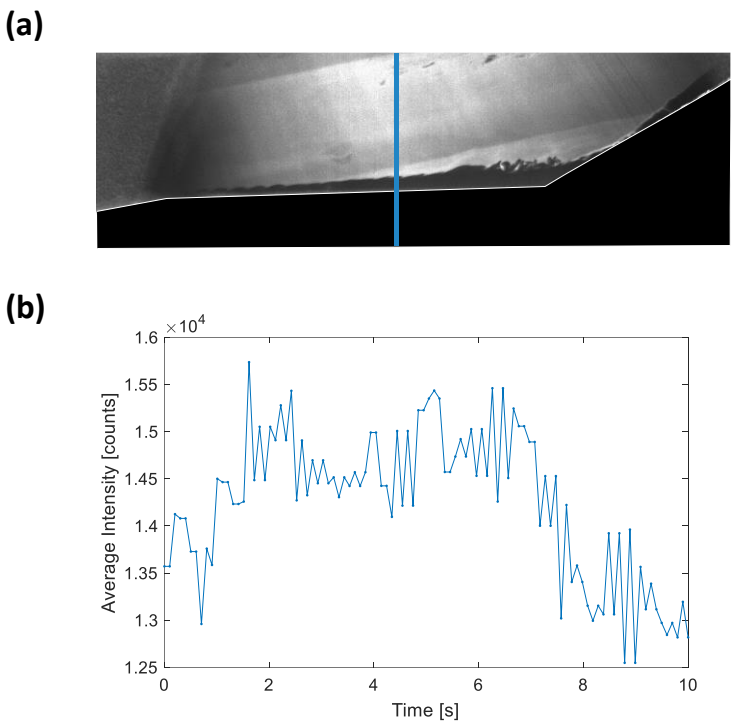

Fig. 5 Sample instantaneous FRS image showing column used for finding average intensity (a) and average intensity (median-filtered) through time showing presence of CO_2 (b).

Using the previous analysis, a total of 70 images were used to find the averages shown in Fig. 6(a). Schlieren images of the cone-slice-ramp geometry were obtained in separate runs, and the average of 10,000 images are shown for comparison to FRS in Fig. 6(b). It must again be noted that schlieren is a path-integrated measurement, while FRS is planar, which will likely result in differences in the images. Additionally, images were not obtained at the same run conditions, but the closest Reynolds numbers were paired as indicated by Table 1. The Reynolds numbers listed in Fig. 6 correspond to conditions for the FRS measurements.

Overall, the scales of flow features such as the conical nose shock, boundary layer, and shear layer are comparable between the FRS and schlieren images. With increasing Reynolds number, the streamwise position of flow separation and reattachment changes drastically. The shear layer thickness at the end of the slice decreased from approximately 22 mm to 11 mm as Reynolds number increases, shown by the dark region in the FRS images indicating the disappearance of CO_2. The flow reattachment subsequently occurs further upstream with increasing Reynolds number, and the reattachment shock appears to match well between FRS and schlieren. For the highest Reynolds number studied, traces of flow turbulence are still observable in the FRS images due to the lack of sufficient averages. If more

samples were available, currently limited by the laser system repetition rate with tunnel run times, then the turbulent fluctuations would be better averaged, as in the schlieren images. The schlieren images appear to show an additional structure within the separation region, which is not visible in the FRS images. Schlieren may be showing the expansion and shear layer separately, while FRS seems to visualize the shear layer only, since the CO_2 has evaporated. This difference can also be seen within the reattachment shock region.

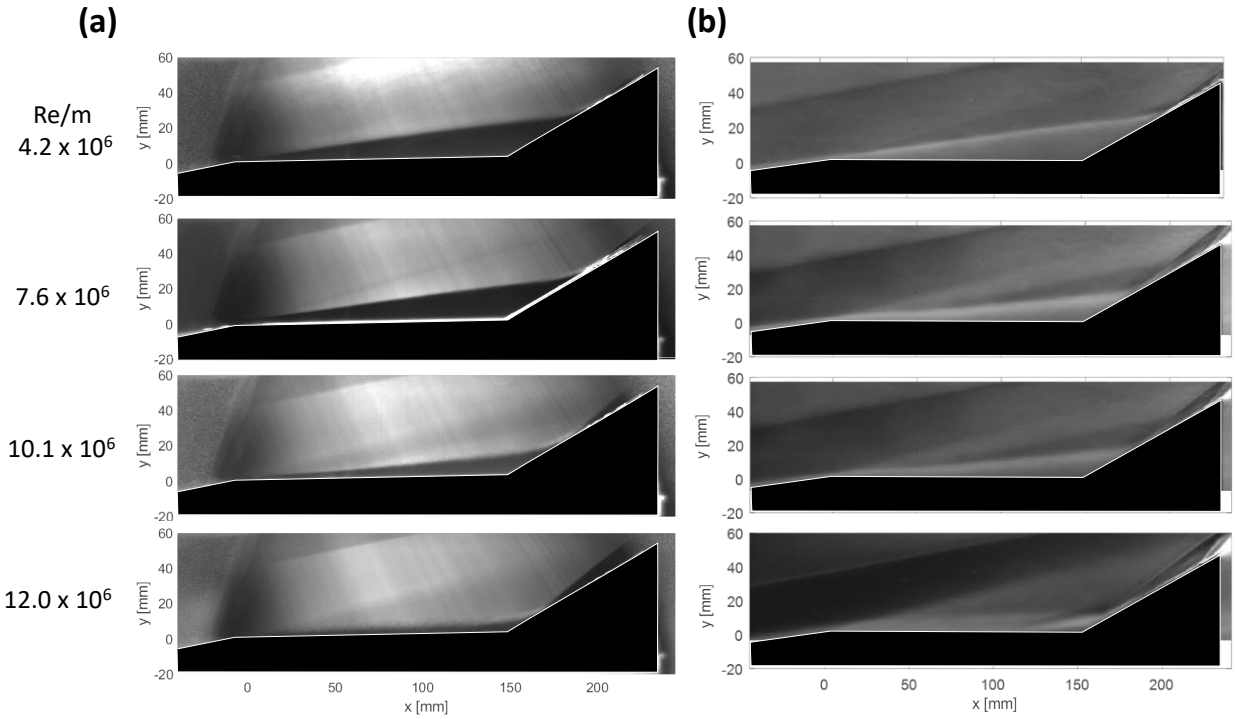

Fig. 6 Average flow images measured by (a) FRS and (b) schlieren for increasing Reynolds number (shown on left for FRS runs). Images were not obtained simultaneously, and the solid white line indicates the surface of the model.

Figure 7 shows instantaneous FRS images of the boundary layer along the slice and ramp for increasing Reynolds number. Two representative instantaneous images (not time-resolved) are shown for each Reynolds number. The lowest Reynolds number studied, Fig. 7(a), shows a predominantly laminar shear layer which separates immediately after encountering the expansion corner of the slice. Large-scale turbulent structures are visible within the conical shock, well away from the model surface, which have previously been observed in PLS experiments and are believed to be from nonuniform CO_2 seeding, or perturbations persisting from the condensation process in the nozzle. With increasing Reynolds number, second mode-like disturbances appear as the shear layer starts to transition to turbulence, Fig. 7(b). The disturbances nearest to the expansion corner have a wavelength of 4 mm. This wavelength corresponds to a frequency near 200 kHz, assuming the phase speed as the edge velocity from the Taylor-Mccoll solution for

conical flow [30]. This frequency shows good agreement to second-mode waves observed in pressure sensor data collected previously using the cone-slice-ramp geometry [5]. These waves can be seen to propagate downstream along the separated shear layer in Fig. 7(b).

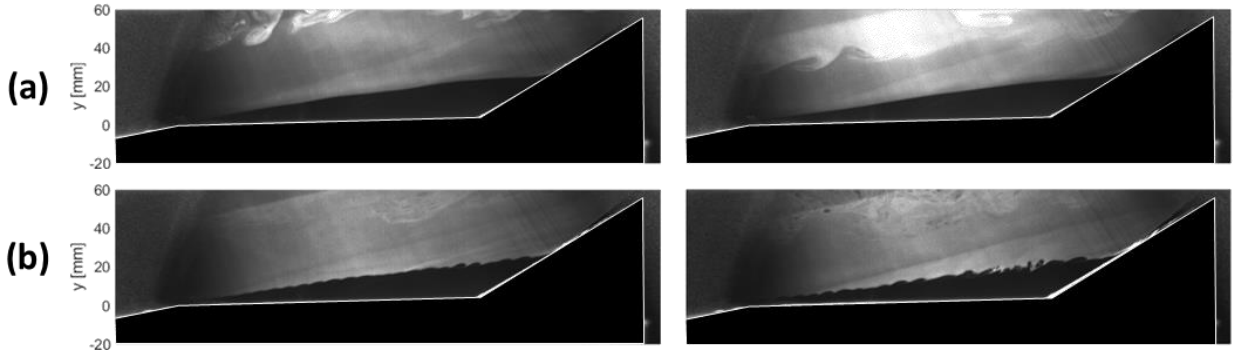

Fig. 7 Instantaneous frames of the flow for Re/m (a) 4.2 × 10^6 and (b) 7.6 × 10^6. The solid white line indicates the surface of the model.

In Fig. 8, three instantaneous images are shown for a transitional Reynolds number of 10.1 × 10^6. With this higher Reynolds number, the boundary layer remains attached on the slice prior to separation. Together, these instantaneous images highlight the unsteadiness of the separation shock. From Fig. 8(a - c), the separation point varies from approximately 90 – 99 mm along the slice. Upon separation, the shear layer continues to transition to turbulence. The scale of turbulent features also appears to impact the shape of the separation shock at this condition. With larger structures, as in Fig. 8(a, d), the shock bulges outward, while it contracts with smaller, flatter features as in Fig. 8(c, f). Fig. 8(f) also appears to show pressure waves emanating from several individual structures. These shaping trends have previously been noted by Bourdon and Dutton, who saw flattening and tilting of turbulence following compression shocks using PLS [12]. The unsteadiness in separation position and shape indicates a likely condition for vibrations and increased pressure loading.

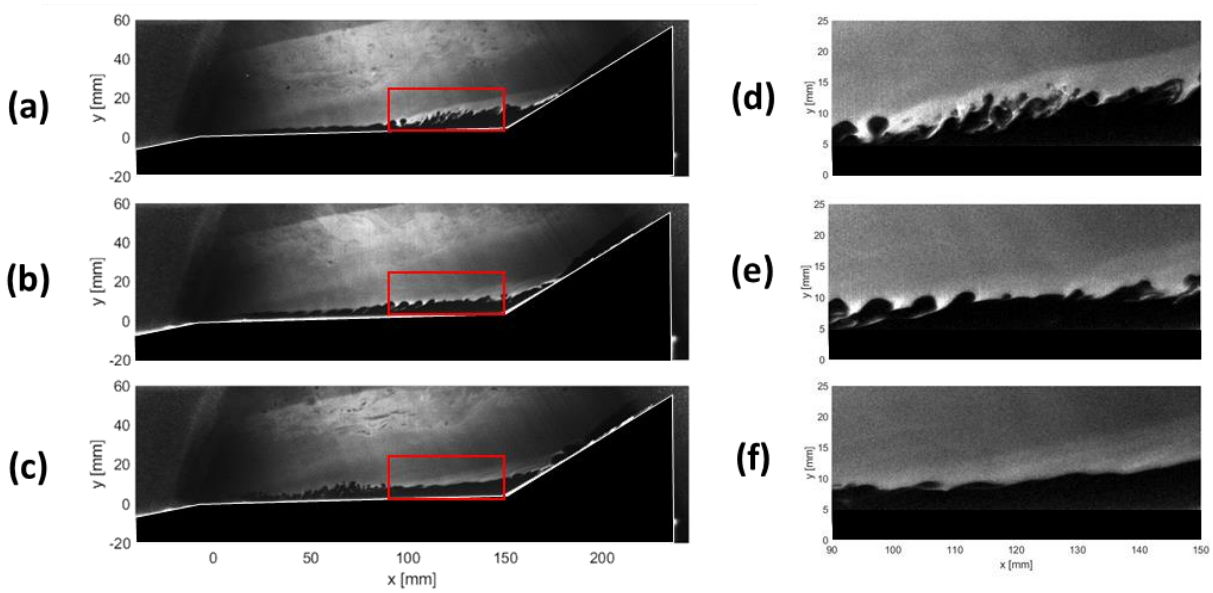

Fig. 8 Instantaneous FRS frames (a – c) for Re/m = 10.1 × 10^6 shown for full field of view. Red box outlines region for zoomed view shown in (d – f). The solid white line indicates the surface of the model.

In the highest Reynolds number studied, Fig. 9 the boundary layer appears fully turbulent and stays attached longer than in Fig. 8. Figure 9(a), the FRS image, clearly shows the separation region beginning near 112 mm, and then reattaching at 18 mm up the ramp. Additionally, the separation region is much smaller for this condition due to the prolonged attachment. Turbulent features are clearly defined in the planar FRS, while the instantaneous schlieren image, Fig. 9(b), integrates the turbulence across the cone-slice, obscuring individual features. Within the reattachment region, turbulence is not visible in the FRS images due to evaporation of CO_2. However, the schlieren image shows turbulent structures along the ramp post reattachment. While the FRS images show turbulence structures with high detail, using the results in combination with pressure sensor data and schlieren imaging can offer more insight into SWBLI.

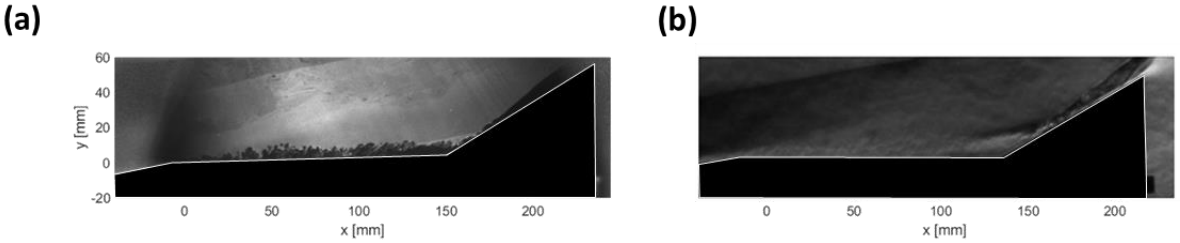

Fig. 9 Instantaneous frames Re/m = 12.0 × 10^6 measured by FRS (a) and high-speed schlieren (b). The solid white line indicates the surface of the model.

IV. Conclusions

In the current work, filtered Rayleigh scattering (FRS) has successfully been applied in the Sandia Hypersonic Wind Tunnel, visualizing the flow over a cone-slice-ramp geometry. Carbon dioxide seeding was used to enhance the Rayleigh scattering signal. Images filtered by the molecular gas filter exhibited strong background rejection, revealing more details of turbulent flow features in the boundary and shear layers. Flow features, such as the boundary layer, shear layer, and separation shock were well-visualized. At lower Reynolds numbers, the flow separated immediately after the expansion corner, while it remained attached with higher Reynolds numbers. At transitional conditions, FRS revealed an unsteady separation region with instantaneous changes to the separation shock structure due to turbulence. A comparison with schlieren images showed flow features of similar scale; however, highly fluctuating, small-scale structures within the reattachment region were not visible in the FRS images due to the lack of surviving CO_2 in this region.

Future improvements to the FRS system may enable imaging in these regions; however, combining current results with high-frequency pressure measurements and schlieren can provide more insight on turbulence transition mechanisms and SWBLI. Additionally, experiments focused on a spanwise FRS measurements will help to probe the three-dimensional separation across the span of the ramp in the future.

Acknowledgments

Sandia National Laboratories is a multi-mission laboratory managed and operated by National Technology and Engineering Solutions of Sandia, LLC., a wholly owned subsidiary of Honeywell International, Inc., for the U.S. Department of Energy's National Nuclear Security Administration under contract DE-NA0003525. The views expressed in the article do not necessarily represent the views of the U.S. Department of Energy or the United States Government.

References

[1] Anderson, J. D. *Hypersonic and high-temperature gas dynamics*: American Institute of Aeronautics and Astronautics Inc., 2019.

[2] Dolling, D. S. "Fifty Years of Shock-Wave/Boundary-Layer Interaction Research: What Next?," *AIAAJ* Vol. 39, No. 8, 2001, pp. 1517-1531.
doi: 10.2514/2.1476

[3] Fedorov, A. "Transition and Stability of High-Speed Boundary Layers," *Annual Review of Fluid Mechanics* Vol. 43, 2011, pp. 79-95.
doi: 10.1146/annurev-fluid-122109-160750

[4] Mack, L. M. "Linear stability theory and the problem of supersonic boundary-layer transition," *AIAAJ* Vol. 13, No. 3, 1975, pp. 278-289.
doi: 10.2514/3.49693
[5] Pandey, A., Casper, K.M., Guildenbecher, D.R., Beresh, S.J., Bhakta, R., De Zetter, M.E., Spillers, R. "Instability Measurements in Hypersonic Flow on a Three-Dimensional Cone-Slice-Ramp Geometry," *AIAA SciTech Forum*. San Diego, CA, 2022, p. 26.
[6] Pandey, A., Casper, K.M., Soehnel, M., Spillers, R.W., Bhakta, R., Beresh, S.J. "Hypersonic Fluid-Structure Interaction on the Control Surface of a Slender Cone," *AIAA SciTech 2021*. Virtual, 2021, p. 29.
[7] Westerweel, J., Elsinga, G.E., Adrian, R.J. "Particle Image Velocimetry for Complex and Turbulent Flows," *Annual Review of Fluid Mechanics* Vol. 45, 2013, pp. 409-436.
doi: 10.1146/annurev-fluid-120710-101204
[8] Beresh, S. J. "Time-resolved particle image velocimetry," *Measurement Science and Technology* Vol. 32, 2021, p. 33.
doi: 10.1088/1361-6501/ac08c5/pdf
[9] Saltzman, A. J., Lowe, K.T., Ng, W.F. "250 kHz three-component Doppler velocimetry at 32 simultaneous points: a new capability for high speed flows," *Meas. Sci. Technol.* Vol. 31, 2020, p. 12.
doi: 10.1088/1361-6501/ab8ee9
[10] Boguszko, M., Elliott, G.S. "On the use of filtered Rayleigh scattering for measurements in compressible flows and thermal fields," *Experiments in Fluids* Vol. 38, 2005, pp. 33-49.
doi: 10.1007/s00348-004-0881-4
[11] Poggie, J., Erbland, P.J., Smits, A.J., Miles, R.B. "Quantitative visualization of compressible turbulent shear flows using condensate-enhanced Rayleigh scattering," *Experiments in Fluids* Vol. 37, 2004, pp. 438-454.
doi: 10.1007/s00348-004-0828-9
[12] Bourdon, C. J., Dutton, J.C. "Planar visualizations of large-scale turbulent structures in axisymmetric supersonic separated flows," *Physics of Fluids* Vol. 11, No. 1, 1999, pp. 201-213.
doi: 10.1063/1.869913
[13] Erbland, P. J., Baumgartner, M.L., Yalin, A.P., Etz, M.R., Muzas, B., Lempert, W.R., Smits, A.J., Miles, R.B. "Development of planar diagnostics for imaging Mach 8 flowfields using carbon dioxide and sodium seeding," AIAA 97-0154, *35th Aerospace Sciences Meeting & Exhibit*. Reno, Nevada, 1997.
[14] Humble, R. A., Peltier, S.J., Bowersox, R.D.W. "Visualization of the structural response of a hypersonic turbulent boundary layer to convex curvature," *Physics of Fluids* Vol. 24, 2012, pp. 106103-1-24.
doi: 10.1063/1.4761833
[15] Saltzman, A. J., Beresh, S.J., Casper, K.M., Denk, B.P., Bhakta, R., De Zetter, M.E., Spillers, R.W. "Carbon Dioxide Seeding System for Enhanced Rayleigh Scattering in Sandia's Hypersonic Wind Tunnel," AIAA 2022-4131, *AIAA Aviation Forum 2022*. Chicago, IL, 2022, p. 19.
[16] Forkey, J. N., Finkelstein, N.D., Lempert, W.R., Miles, R.B. "Demonstration and characterization of filtered Rayleigh scattering for planar velocity measurements," *AIAAJ* Vol. 34, No. 3, 1996, pp. 442-448.
doi: 10.2514/3.13087
[17] Beresh, S. J., Casper, K.M., Wagner, J.L., Henfling, J.H., Spillers, R.W., Pruett, B.O. "Modernization of Sandia's Hypersonic Wind Tunnel," *53rd AIAA Aerospace Sciences Meeting*. Kissimmee, Florida, 2015, p. 1338.
[18] Casper, K. M., Beresh, S.J., Henfling, J.H., Spillers, R.W., Pruett, B.O., Schneider, S.P. "Hypersonic Wind-Tunnel Measurements of Boundary-Layer Transition on a Slender Cone," *AIAAJ* Vol. 54, No. 4, 2016, pp. 1250-1263.
doi: 10.2514/1.J054033
[19] Erbland, P. J., Rizzetta, D.P., Miles, R.B. "Numerical and experimental investigation of CO2 condensate behavior in hypersonic flow," AIAA 2000-2379, *21st Aerodynamic Measurement Technology and Ground Testing Conference*. Denver, CO, 2000, p. 24 pp.
[20] Pandey, A., Schmidt, B.E., Lynch, K.P., Casper, K.M., Beresh, S.J., Bhakta, R., Downing, C., DeZetter, M.E., Spillers, R. "Demonstration of Internal Digital Image Correlation for Fluid-Structure Interaction Measurements in a Hypersonic Wind Tunnel," AIAA 2022-3561, *AIAA Aviation 2022 Forum*. Chicago, IL, 2022.
[21] Forkey, J. N., Lempert, W.R., Miles, R.B. "Corrected and calibrated I2 absorption model at frequency-doubled Nd:YAG laser wavelengths," *Appl Opt* Vol. 36, 1997, pp. 6729-38.
doi: 10.1364/AO.36.006729
[22] Cadel. D.R., L., K.T. "Cross-correlation Doppler global Velocimetry (CC-DGV)," *Opt. Las. Eng.* Vol. 71, 2015, pp. 51-61.
doi: 10.1016/j.optlaseng.2015.03.012
[23] Saltzman, A. J., Beresh, S.J., Kearney, S.P., Crabtree, C.Q., Slipchenko, M. "Toward Snapshot Cross-Correlation Doppler Global Velocimetry for High-Speed Flows," *AIAA SciTech 2022*. San Diego, CA, 2022, p. 17.
[24] Tenti, G., Boley, C.D., Desai, R.C. "On the kinetic model description of Rayleigh–Brillouin scattering from molecular gases," *Can. J. Phys.* Vol. 52, 1974, pp. 285-90.
doi: 10.1139/p74-041
[25] Pan, X., Shneider, M.N., Miles, R.B. "Coherent Rayleigh-Brillouin scattering in molecular gases," *Phys. Rev. A* Vol. 69, 2004, p. 033814.
doi: 10.1103/PhysRevA.69.033814

[26] Boyda, M. T., Byun. G., Saltzman, A.J., Lowe, K.T. "Influence of Mie and Geometric Scattering on Temperature and Density Measurements in Filtered Rayleigh Scattering," AIAA 2020-1516, *AIAA SciTech Forum 2020*. Orlando, FL, 2020, p. 16.
[27] Elliott, G. S., Glumac, N., Carter, C.D. "Molecular filtered Rayleigh scattering applied to combustion," *Meas. Sci. Technol.* Vol. 12, 2001, pp. 452-66.
doi: 10.1088/0957-0233/12/4/309
[28] Mielke, A. F., Seasholtz, R.G., Elam, K.A., Panda, J. "Time-average measurement of velocity, density, temperature, and turbulence velocity fluctuations using Rayleigh and Mie scattering," *Experiments in Fluids* Vol. 39, 2005, pp. 441-454.
doi: 10.1007/s00348-005-0990-8
[29] Saltzman, A. J., Boyda, M.T., Lowe, K.T., Ng, W.F. "Filtered Rayleigh Scattering for Velocity and Temperature Measurements of a Heated Supersonic Jet with Thermal Non-Uniformity," AIAA 2019-2677, *25th AIAA/CEAS Aeroacoustics Conference*. Delft, The Netherlands, 2019, p. 15.
[30] Anderson, J. D. *Modern Compressible Flow: With Historical Perspective*: McGraw Hill, 1990.